

Transport-based imaging in random media

Guillaume Bal* Kui Ren†

April 30, 2007

Abstract

This paper derives a radiative transfer equation from first principles to model the energy density of (mono-frequency) high frequency waves propagating in a random medium composed of localized scatterers. The correlation length of the random scatterers is small compared to the overall distance of propagation so that ensemble averaging may take place.

The paper also considers the detection and imaging of inclusions buried in highly scattering random media. In such multiple scattering environments, the coherent wave fields may be too weak to be used for imaging purposes. We thus propose to model the inclusions as parameters in the macroscopic radiative transfer equations and consider the imaging problem as an inverse transport problem.

Numerical simulations address the domain of validity of the radiative transfer equation and of the imaging method. Wave propagation is solved by using a Foldy-Lax framework and the forward and inverse transport problems are solved by using a Monte Carlo method. Since the inverse transport problem is ill-posed, the buried inclusions are parameterized by a small number of degrees of freedom, typically their position and a few geometric properties.

Key words. Imaging in random media, high frequency waves in random media, inverse problems, radiative transfer equation, Foldy-Lax model

1 Introduction

The imaging of inclusions buried in random media from acoustic, electromagnetic, or elastic wave measurements has a long history. We refer the reader to e.g. [2, 7, 13, 19, 28, 26, 34] and their reference. Several imaging methods have been proposed based on the type of available data and on the regime of wave propagation.

The most favorable situation occurs when the specific realization of the random medium is known explicitly. We can then use the refocusing properties of time reversed waves to backpropagate measured wave fields numerically through the known random environment. The time reversed waves focus at the location of the buried inclusions and

*Department of Applied Physics & Applied Mathematics, Columbia University, New York, NY 10027; gb2030@columbia.edu; <http://www.columbia.edu/~gb2030>

†Department of Applied Physics & Applied Mathematics, Columbia University, New York, NY 10027; kr2002@columbia.edu; <http://www.columbia.edu/~kr2002>

allow for fairly accurate imaging; see e.g. [10, 12, 22]. Note however that even small errors in the assessment of the random medium, such as the mis-location of the random scatterers by an amount comparable to the typical wavelength of the propagating waves, have a very large effect on the refocusing of time-reversed waves [11, 29].

In most applications, however, the random medium is not known and this lack of knowledge inevitably degrades the quality of the reconstructions. Randomness may then roughly be treated in two different ways. One may either assume that noise is sufficiently small so that it may be treated perturbatively. Imaging is then performed by backpropagating appropriately mollified wave field measurements into a homogeneous medium or a medium with smooth variations, whose determination is often an important aspect of the reconstruction. One of the main pitfall in such reconstructions is that many classical inversion techniques are not statistically stable, i.e., the reconstruction strongly depends on the realization in a given set of random media. We refer the reader to e.g. [13] for optimal, statistically stable, imaging methods in that context. Such methods however cannot work when the fluctuations in the random medium increase to a point where the coherent wave field, i.e., the part of the wave field that is not affected by random scattering, becomes too weak. In such regimes of strong scattering, other models are necessary.

The alternative to backpropagation in a homogeneous or smoothly varying medium is to find a model that describes wave propagation in the random medium. In regimes where the wavelength and the correlation length of the random medium are very small compared to the overall distance of propagation, such as in the propagation of light through the atmosphere or of near-infra-red photons through human tissues, the kinetic description for wave propagation is extremely accurate [1, 16]. The wave energy density is then modeled quite accurately by a radiative transfer (transport) equation or a diffusion equation.

In this paper, we are interested in the validity of the radiative transfer model in a more intermediate regime, where the fluctuations in the random medium are too strong for imaging methods based on coherent information to work, and where the typical wavelength in the system is smaller, though not orders of magnitude smaller, than the overall distance of propagation. Typically, we could have GHz microwaves, with a wavelength of 30cm, propagate over distances of tens or hundreds of meters. The typical random medium we consider here is made of hundreds of scatterers, with a mean separation distance between scatterers comparable or large compared to the wavelength but small compared to the overall distance of propagation. Our objective is then to detect and image a -sufficiently large- inclusion buried in the random medium.

When the density of scatterers is sufficiently large so that the coherent wave field is too weak to be useful in imaging, the incoherent part of the wave field, i.e., the part that has interacted with the unknown random medium, can no longer be neglected and needs to be modeled. Such a model has to depend on the regime of wave propagation. In the high frequency regime, when the wavelength is smaller than the propagation distance, the simplest extension of wave propagation in homogeneous domains is arguably the radiative transfer equation. Such an equation models the propagation of the phase-space energy density $a(t, \mathbf{x}, \mathbf{k})$ at time t , position \mathbf{x} , and wave number \mathbf{k} and for acoustic waves

takes the form

$$\frac{\partial a}{\partial t} + c\hat{\mathbf{k}} \cdot \nabla_{\mathbf{x}} a = \mathcal{Q}a, \quad \mathcal{Q}a = \int_{\mathbb{R}^d} \sigma(\mathbf{x}, \mathbf{k}', \mathbf{k})(a(t, \mathbf{x}, \mathbf{k}') - a(t, \mathbf{x}, \mathbf{k}))\delta(c|\mathbf{k}'| - c|\mathbf{k}|)d\mathbf{k}', \quad (1)$$

where $\hat{\mathbf{k}} = \mathbf{k}/|\mathbf{k}|$, c is sound speed, and $\sigma(\mathbf{x}, \mathbf{k}, \mathbf{k}')$ is the scattering coefficient, which is inversely proportional to the mean free path, the mean distance between successive interactions of the wave energy with the underlying medium. Note that the radiative transfer equation may be seen as a perturbation of the propagation of high frequency waves in a homogeneous medium, which corresponds to the case $\sigma = 0$. The radiative transfer equation is thus characterized by two features: scattering is not sufficiently strong to modify the advection nature of high frequency waves; this is the left hand side in (1). However, because of incoherent interactions with the underlying structure, the -partially incoherent- energy density, rather than the wave field, needs to be modeled, and while the energy density still transport through the random medium, it does so by possibly changing direction in a way described by the scattering operator on the right-hand side of (1). In that sense, it may be seen as the simplest model for the energy density of high-frequency waves propagating in heterogeneous media.

Radiative transfer equations have also been extensively studied and derived either phenomenologically or from first principles (as an approximation to a wave equation); see [3, 16, 21, 25, 33, 35, 36]. We rederive the equation in the setting of localized (possibly) strong scatterers adapting techniques in [3, 33] to model the energy density of mono-frequency waves propagating in such a random medium. The localized scatterers are assumed here to have a Poisson distribution. We then propose to assess the range of validity of the radiative transfer model by comparing its predictions with wave field calculations. We use a Foldy-Lax model to compute the wave fields. We demonstrate based on numerical simulations that the radiative transfer equations are very accurate provided that the wave energy measurements are sufficiently stable statistically.

Statistical stability is a cornerstone in the interferometric imaging techniques developed in [13]. Reconstructions based on coherent information are much enhanced when a carefully calibrated to the random medium, statistically stable, inversion technique is employed. When macroscopic models for the incoherent energy density are used, statistical stability is an absolute prerequisite to any form of imaging. It is impossible, based on one measurement, to image an inclusion whose influence on the detectors is a random variable whose fluctuations cannot be averaged out one way or another (for instance by collecting measurements on a larger detector). It turns out that in the high frequency limit, wave energy densities are indeed statistically stable for a wide class of random media. This has been proved in simplified models of wave propagation [5, 6] and has been confirmed numerically [8, 9].

We present here numerical evidence of the statistical stability of the wave energy density in sufficiently mixing random media with localized scatterers. What we mean by sufficiently mixing is that the density of scatterers is sufficiently high. We demonstrate numerically the physically simple fact that the energy density is more stable statistically when the density of scatterers increases (their correlation length decreases) while their scattering strength decreases in such a way that the mean free path remains constant.

Once we are confident in the radiative transfer equation as a model for the wave energy density, we use the model to image buried inclusions in such random media. We

assume here that the random medium is statistically homogeneous, i.e., that its statistics are invariant by translation. We can consider two scenarios. In the first scenario, we measure energy densities in the presence of the inclusion. We thus have to estimate the mean free path of the random medium and image the inclusion at the same time. In such a configuration, the inclusion's influence on available measurements has to be larger than the statistical instability coming from our lack of knowledge of the underlying random medium. In the second scenario, we have access to energy measurements in the presence *and* in the absence of the inclusion. We may thus perform differential measurements. These differential measurements are then obviously proportional to the inclusion. With a kinematic picture in mind, all the instability in the random paths that do not visit the object cancel out in differential measurements, thus allowing us to image much smaller objects. We consider reconstructions under these two scenarios based on forward wave field calculations and inverse transport problems.

The rest of the paper is structured as follows. Section 2 presents our model of random media with localized scatterers and derives the radiative transfer equation from a high-frequency acoustic wave equation. Time-dependent and mono-frequency equations are considered. The Foldy-Lax approximation to wave propagation is also presented. The numerical validation of the radiative transfer equations based on Foldy-Lax wave simulations and transport Monte Carlo simulations is presented in Section 3. Transport-based imaging of inclusions in random media is then considered in Section 4.

2 Radiative transfer models

In this section, we introduce the microscopic and macroscopic models for the propagation of high frequency waves in random media with localized scatterers.

We start from the acoustic wave equation with sound speed given by the superposition of a constant background sound speed and localized strong fluctuations. The radiative transfer equation is obtained as the high frequency limit of the energy density of the acoustic waves following methods developed in e.g. [3, 33] in Section 2.1. The corresponding transport equation for mono-frequency (time-harmonic) waves is given in Section 2.2. Because the scatterers are localized on a scale much smaller than the wavelength, the wave equation for time-harmonic wave fields is approximated by the Foldy-Lax model, which is recalled in Section 2.3.

It remains to address the modeling of the buried inclusions. Extended objects are treated like any other point-like object in the Foldy Lax formalism. At the radiative transfer level, we assume that the inclusion is sufficiently large compared to the wavelength so that energy reflects specularly at the inclusion's boundary. Such models are explained in greater detail in Section 2.4.

2.1 Derivation of the transport equation

We consider the propagation of scalar waves in media with constant (to simplify) density ρ_0 and spatially varied compressibility $\kappa(\mathbf{x})$

$$\rho_0 \partial_t \mathbf{v} + \nabla p = 0, \quad \kappa(\mathbf{x}) \partial_t p + \nabla \cdot \mathbf{v} = 0, \quad p(0, \mathbf{x}) = p_0(\mathbf{x}), \quad \mathbf{v}(0, \mathbf{x}) = \mathbf{v}_0(\mathbf{x}), \quad (2)$$

where $t > 0$ and $\mathbf{x} \in \mathbb{R}^d$ with $d \geq 2$ the spatial dimension. The theories that follow generalize to the context of electromagnetic and elastic waves; see e.g. [3, 33]. We restrict ourselves to the case of acoustic waves for concreteness.

In the high frequency regime of interest in this paper, the above equation rescales, after the change of variables $t \mapsto \frac{t}{\varepsilon}$ and $\mathbf{x} \mapsto \frac{\mathbf{x}}{\varepsilon}$, as

$$\rho_0 \varepsilon \partial_t \mathbf{v}_\varepsilon + \varepsilon \nabla p_\varepsilon = 0, \quad \kappa_\varepsilon(\mathbf{x}) \varepsilon \partial_t p_\varepsilon + \varepsilon \nabla \cdot \mathbf{v}_\varepsilon = 0, \quad (3)$$

where the initial conditions $p_\varepsilon(0, \mathbf{x}) = p_{0\varepsilon}(\mathbf{x})$ and $\mathbf{v}_\varepsilon(0, \mathbf{x}) = \mathbf{v}_{0\varepsilon}(\mathbf{x})$ oscillate at the frequency ε^{-1} . The parameter ε thus models the typical wavelength in the system. The wave speed is defined as

$$c_\varepsilon^2(\mathbf{x}) = \frac{1}{\rho_0 \kappa_\varepsilon(\mathbf{x})} = c_0^2(\mathbf{x}) - \sqrt{\varepsilon} V_\varepsilon\left(\frac{\mathbf{x}}{\varepsilon}\right). \quad (4)$$

We retain the scaling $\sqrt{\varepsilon} V_\varepsilon(\frac{\mathbf{x}}{\varepsilon})$ to use the results developed in e.g. [3, 33]. Neither the amplitude nor the correlation length of the potential V_ε are necessarily of order $O(1)$ however. More precisely, the potential V_ε is chosen as

$$V_\varepsilon(\mathbf{x}) = \varepsilon^{-\frac{(\gamma+\beta)d}{2}} \sum_j \tau_j V\left(\frac{\mathbf{x} - \mathbf{x}_j^\varepsilon}{\varepsilon^\beta}\right), \quad (5)$$

where $\beta > 0$, $\gamma < 1$, where $V(\mathbf{x})$ is a compactly supported non-negative, uniformly bounded, function, where the points $\mathbf{x}_j^\varepsilon(\omega)$ form a Poisson point process of density $\nu_\varepsilon = \varepsilon^{\gamma d} n_0$, and where the coefficients $\tau_j(\omega)$ are square-integrable, mean-zero, independent identically distributed random variables. Here ω is a point in a sufficiently large abstract probability space (Ω, \mathcal{F}, P) .

The sound speed fluctuations are therefore of the form

$$\sqrt{\varepsilon} V_\varepsilon\left(\frac{\mathbf{x}}{\varepsilon}\right) = \varepsilon^{\frac{1-(\gamma+\beta)d}{2}} \sum_j \tau_j V\left(\frac{\mathbf{x} - \varepsilon \mathbf{x}_j^\varepsilon}{\varepsilon^{1+\beta}}\right). \quad (6)$$

We thus conclude that the thickness of the scatterers is $t_\varepsilon = \varepsilon^{1+\beta} \ll \varepsilon$, the correlation length in the medium is $l_\varepsilon = \varepsilon^{1-\gamma} L$ for L a typical distance of propagation, which verifies $l_\varepsilon \gg \varepsilon$ when $0 < \gamma < 1$ and $L = O(1)$, and the density of scatterers is $n_\varepsilon = \varepsilon^{-d} \nu_\varepsilon = \varepsilon^{(\gamma-1)d} n_0 \gg O(1)$.

Note that Poisson point process allow the clustering of points \mathbf{x}_j^ε , although the number of points in a given bounded domain is bounded P -a.s. There is therefore a (P -)small subset Ω_ε of Ω where the above fluctuation is larger than c_0^2 , which would result in a negative c_ε^2 . The process in (6) thus needs to be modified on Ω_ε , for instance by setting the fluctuations to 0. We verify, although we shall not present this here, that such modifications of the process in (6) occur on a very small set and that the calculations of the power spectra presented below are not affected by the change.

We can now use the results obtained in [33] to show that the wave energy density is such that

$$\mathcal{E}_\varepsilon(t, \mathbf{x}) - \int_{\mathbb{R}^d} a_\varepsilon(t, \mathbf{x}, \mathbf{k}) d\mathbf{k} \rightarrow 0, \quad (7)$$

in a weak sense (i.e., after integration against a test function in the spatial variables \mathbf{x}), where $\mathcal{E}_\varepsilon(t, \mathbf{x})$ is the energy density defined as

$$\mathcal{E}_\varepsilon(t, \mathbf{x}) = \rho_0 |\mathbf{v}_\varepsilon|^2(t, \mathbf{x}) + \kappa_\varepsilon(\mathbf{x}) p_\varepsilon^2(t, \mathbf{x}), \quad (8)$$

and where $a_\varepsilon(t, \mathbf{x}, \mathbf{k})$ is a phase-space energy density, which solves the following radiative transfer equation

$$\frac{\partial a_\varepsilon}{\partial t} + c_0 \hat{\mathbf{k}} \cdot \nabla a_\varepsilon = \int_{\mathbb{R}^d} \sigma_\varepsilon(\mathbf{x}, \mathbf{k}, \mathbf{q}) (a_\varepsilon(\mathbf{x}, \mathbf{q}) - a_\varepsilon(\mathbf{x}, \mathbf{k})) \delta(c_0 |\mathbf{k}| - c_0 |\mathbf{q}|) d\mathbf{q}, \quad (9)$$

with appropriate initial conditions, where

$$\sigma_\varepsilon(\mathbf{x}, \mathbf{k}, \mathbf{q}) = \frac{\pi c_0^2 |\mathbf{k}|^2}{2(2\pi)^d} \hat{R}_\varepsilon(\mathbf{k} - \mathbf{q}). \quad (10)$$

Here, \hat{R}_ε is the power spectrum of the fluctuations V_ε . It is the Fourier transform of the correlation function R_ε of the fluctuations V_ε . They are defined as follows:

$$\begin{aligned} c_0^4 R_\varepsilon(\mathbf{y}) &= \mathbb{E}\{V_\varepsilon(\mathbf{x})V_\varepsilon(\mathbf{x} + \mathbf{y})\} \\ (2\pi)^d c_0^4 \hat{R}_\varepsilon(\mathbf{p}) \delta(\mathbf{p} + \mathbf{q}) &= \mathbb{E}\{\hat{V}_\varepsilon(\mathbf{p})\hat{V}_\varepsilon(\mathbf{q})\}, \end{aligned} \quad (11)$$

where $\hat{V}_\varepsilon(\mathbf{p}) = \int_{\mathbb{R}^d} e^{-i\mathbf{x} \cdot \mathbf{p}} V_\varepsilon(\mathbf{x}) d\mathbf{x}$ is the Fourier transform of $V_\varepsilon(\mathbf{x})$. We then have the following result on the asymptotic limit of the power spectrum.

Lemma 2.1. *Let us assume that $V(\mathbf{x})$ is a non-negative, integrable, compactly supported function such that $\hat{V}(\mathbf{0}) = c_0^4 L^d$ for some characteristic distance $0 < L = O(1)$, where $\hat{V}(\mathbf{k})$ is the Fourier transform of V . Then we find that the power spectrum $\hat{R}_\varepsilon(\mathbf{k})$ converges in the uniform norm uniformly on compact sets to the limit*

$$\hat{R}_0 = L^{2d} \mathbb{E}\{\tau^2\} n_0. \quad (12)$$

Proof. We calculate that

$$c_0^4 R_\varepsilon(\mathbf{y}) = \varepsilon^{-(\gamma+\beta)d} \mathbb{E}\{\tau^2\} \mathbb{E}\left\{ \sum_{j=1}^{\infty} V\left(\frac{\mathbf{x} - \mathbf{x}_\varepsilon^j}{\varepsilon^\beta}\right) V\left(\frac{\mathbf{x} + \mathbf{y} - \mathbf{x}_\varepsilon^j}{\varepsilon^\beta}\right) \right\}.$$

Since V is compactly supported, there is a domain D , at \mathbf{x} and \mathbf{y} fixed, such that the above product vanishes for \mathbf{x}_ε^j outside of D . The Poisson point processes verifies that the number of points on D satisfies a Poisson distribution and that conditioned on the number of points, these points are uniformly and independently distributed on D . This yields that

$$\begin{aligned} & \mathbb{E}\left\{ \sum_{j=1}^{\infty} V\left(\frac{\mathbf{x} - \mathbf{x}_\varepsilon^j}{\varepsilon^\beta}\right) V\left(\frac{\mathbf{x} + \mathbf{y} - \mathbf{x}_\varepsilon^j}{\varepsilon^\beta}\right) \right\} \\ &= \sum_{m=0}^{\infty} e^{-|D|\nu_\varepsilon} \frac{(|D|\nu_\varepsilon)^m}{m!} \sum_{j=1}^m \int_D V\left(\frac{\mathbf{x} - \mathbf{z}}{\varepsilon^\beta}\right) V\left(\frac{\mathbf{x} + \mathbf{y} - \mathbf{z}}{\varepsilon^\beta}\right) \frac{d\mathbf{z}}{|D|} \\ &= \nu_\varepsilon \int_{\mathbb{R}^d} V\left(\frac{\mathbf{z} - \mathbf{x}}{\varepsilon^\beta}\right) V\left(\frac{\mathbf{z} - \mathbf{x} - \mathbf{y}}{\varepsilon^\beta}\right) d\mathbf{z}, \end{aligned}$$

where $|D|$ is the Lebesgue measure of D . Now,

$$\begin{aligned} H_\varepsilon(\mathbf{y}) &= \int_D V\left(\frac{\mathbf{z}-\mathbf{x}}{\varepsilon^\beta}\right) V\left(\frac{\mathbf{z}-\mathbf{x}-\mathbf{y}}{\varepsilon^\beta}\right) d\mathbf{z} = \frac{1}{(2\pi)^d} \int_{\mathbb{R}^d} e^{-i\frac{\mathbf{x}\cdot\mathbf{k}}{\varepsilon^\beta}} e^{i\frac{(\mathbf{x}+\mathbf{y})\cdot\mathbf{k}}{\varepsilon^\beta}} |\hat{V}(\mathbf{k})|^2 d\mathbf{k} \\ &= \frac{1}{(2\pi)^d} \int_{\mathbb{R}^d} e^{i\mathbf{y}\cdot\mathbf{k}} \varepsilon^{\beta d} |\hat{V}(\varepsilon^\beta \mathbf{k})|^2 d\mathbf{k}. \end{aligned}$$

Its Fourier transform is thus given by

$$\hat{H}_\varepsilon(\mathbf{p}) = \varepsilon^{\beta d} |\hat{V}(\varepsilon^\beta \mathbf{p})|^2 = \varepsilon^{\beta d} (|\hat{V}(\mathbf{0})|^2 + O(\varepsilon^\beta)),$$

where $O(\varepsilon^\beta)$ means a term of order ε^β in the uniform norm, uniformly bounded on compact sets. This follows e.g. from the analyticity of $\hat{V}(\mathbf{p})$. Since $\hat{R}_\varepsilon(\mathbf{k})$ is the Fourier transform of $R_\varepsilon(\mathbf{x})$, we find that

$$c_0^4 \hat{R}_\varepsilon(\mathbf{k}) = (|\hat{V}(\mathbf{0})|^2 + O(\varepsilon^\beta)) \mathbb{E}\{\tau^2\} n_0.$$

This proves the result. \square

In the limit $\varepsilon \rightarrow 0$, we thus find that a_ε converges to the solution of the following radiative transfer equation:

$$\frac{\partial a}{\partial t} + c_0 \hat{\mathbf{k}} \cdot \nabla a + \Sigma(\mathbf{x}, |\mathbf{k}|) a = \int_{\mathbb{R}^d} \sigma(\mathbf{x}, \mathbf{k}, \mathbf{q}) a(t, \mathbf{x}, \mathbf{q}) \delta(c_0 |\mathbf{k}| - c_0 |\mathbf{q}|) d\mathbf{q}, \quad (13)$$

where

$$\begin{aligned} \sigma(\mathbf{x}, \mathbf{k}, \mathbf{q}) &= \frac{\pi |\mathbf{k}|^2 L^{2d} c_0^2 \mathbb{E}\{\tau^2\} n_0}{2(2\pi)^d} \\ \Sigma(\mathbf{x}, |\mathbf{k}|) &= \frac{|S^{d-1}| \pi}{2(2\pi)^d} |\mathbf{k}|^{d+1} L^{2d} c_0 \mathbb{E}\{\tau^2\} n_0. \end{aligned} \quad (14)$$

Here, $|S^{d-1}|$ is the Lebesgue measure of the unit sphere in \mathbb{R}^d .

Note that the transport equations generalize to the case where the density of scatterers depends on space. For instance, we may assume that the sound speed fluctuations are of the form

$$\sqrt{\varepsilon} V_\varepsilon(\mathbf{x}, \frac{\mathbf{x}}{\varepsilon}) = \varepsilon^{\frac{1-(\gamma+\beta)d}{2}} \sum_j \tau_j \varphi(\mathbf{x}_j^\varepsilon) V\left(\frac{\mathbf{x} - \varepsilon \mathbf{x}_j^\varepsilon}{\varepsilon^{1+\beta}}\right), \quad (15)$$

where $\varphi(\mathbf{x})$ is a deterministic non-negative function on \mathbb{R}^d . In the numerical simulations considered below, $\varphi(\mathbf{x})$ is the indicatrix function of our computational domain. The limit in (12) is then modified as

$$\hat{R}_0(\mathbf{x}) = \varphi^2(\mathbf{x}) L^{2d} \mathbb{E}\{\tau^2\} n_0. \quad (16)$$

The scattering coefficients in (14) also need be multiplied by $\varphi^2(\mathbf{x})$ and thus become spatially dependent.

2.2 Transport equation in the frequency domain

The derivation of transport equations for mono-frequency waves cannot be deduced in a straightforward way from time-dependent equations. We refer to [15] for a derivation of kinetic models from the Helmholtz equation. We formally generalize these results by adding a scattering operator to the transport equation to model the interaction with the underlying random medium.

The Helmholtz equation for the mono-frequency wave field $u_\varepsilon(\mathbf{x})$ with high frequency $\frac{\omega}{\varepsilon}$ takes the form:

$$\varepsilon^2 \Delta u_\varepsilon(\mathbf{x}) + \frac{\omega^2}{c_\varepsilon^2(\mathbf{x})} u_\varepsilon(\mathbf{x}) = \frac{1}{\varepsilon^{\frac{d-1}{2}}} \varphi\left(\frac{\mathbf{x} - \mathbf{x}_0}{\varepsilon}\right), \quad (17)$$

where $\varphi(\mathbf{x})$ is a smooth function which localizes in the vicinity of the point \mathbf{x}_0 . We assume that the density of scatterers vanishes in the vicinity of the source location \mathbf{x}_0 so that the dispersion relation is $\omega = c_0|\mathbf{k}|$ locally.

In the absence of scatterers, the results obtained e.g. in [15] show that there exists a positive bounded measure $a(\mathbf{x}, \mathbf{k})$ such that

$$\lim_{\varepsilon \rightarrow 0} |u_\varepsilon(\mathbf{x})|^2 := \nu(\mathbf{x}) = \int_{\mathbb{R}^d} a(\mathbf{x}, \mathbf{k}) d\mathbf{k}, \quad (18)$$

where $\nu(\mathbf{x})$ is a positive measure on \mathbb{R}^d . Moreover the phase-space measure $a(\mathbf{x}, \mathbf{k})$ solves the Liouville equation:

$$c_0 \hat{\mathbf{k}} \cdot \nabla a = Q(\mathbf{x}, \mathbf{k}), \quad (19)$$

with the source $Q(\mathbf{x}, \mathbf{k})$ given by

$$\begin{aligned} Q(\mathbf{x}, \mathbf{k}) &= \frac{c_0^2}{2\omega(2\pi)^{d-1}} \delta(\mathbf{x} - \mathbf{x}_0) \delta\left(\frac{\omega^2}{c_0^2} - |\mathbf{k}|^2\right) |\hat{\varphi}(\mathbf{k})|^2 \\ &= \frac{c_0^3}{4\omega^2(2\pi)^{d-1}} \delta(\mathbf{x} - \mathbf{x}_0) \delta\left(\frac{\omega}{c_0} - |\mathbf{k}|\right) |\hat{\varphi}(\mathbf{k})|^2. \end{aligned} \quad (20)$$

The above transport equation should be augmented with outgoing radiation conditions, namely the incoming field $a(\mathbf{x} - t\mathbf{k}, \mathbf{k}) \rightarrow 0$ as $t \rightarrow +\infty$.

We briefly recall the derivation of the above equation and explain the scaling for the source term in (17). The regularized Helmholtz equation (17) with constant sound speed may be written as

$$(i\varepsilon\alpha + \varepsilon^2 \Delta + \frac{\omega^2}{c_0^2}) u_\varepsilon = \frac{1}{\varepsilon^{\frac{d-1}{2}}} \varphi\left(\frac{\mathbf{x}}{\varepsilon}\right),$$

for some causality-preserving regularization parameter $0 < \alpha \ll 1$, and where we set $\mathbf{x}_0 = 0$ to simplify the presentation. In the Fourier domain at frequency $\boldsymbol{\xi}/\varepsilon$, this is

$$\hat{u}_\varepsilon\left(\frac{\boldsymbol{\xi}}{\varepsilon}\right) = \frac{\varepsilon^d \varepsilon^{-\frac{d-1}{2}} \hat{\varphi}(\boldsymbol{\xi})}{i\varepsilon\alpha + \frac{\omega^2}{c_0^2} - |\boldsymbol{\xi}|^2}.$$

Let us now introduce the Wigner transform of u_ε :

$$W_\varepsilon(\mathbf{x}, \mathbf{k}) = \frac{1}{(2\pi)^d} \int_{\mathbb{R}^d} u_\varepsilon\left(\mathbf{x} - \frac{\varepsilon\mathbf{y}}{2}\right) u_\varepsilon^*\left(\mathbf{x} + \frac{\varepsilon\mathbf{y}}{2}\right) e^{i\mathbf{k}\cdot\mathbf{y}} d\mathbf{y},$$

which verifies that

$$|u_\varepsilon(\mathbf{x})|^2 = \int_{\mathbb{R}^d} W_\varepsilon(\mathbf{x}, \mathbf{k}) d\mathbf{k}.$$

We verify that the Fourier transform $\mathbf{x} \rightarrow \mathbf{q}$ of W_ε is given by

$$\begin{aligned} \hat{W}_\varepsilon(\mathbf{q}, \mathbf{k}) &= \frac{1}{(2\pi\varepsilon)^d} \hat{u}_\varepsilon\left(\frac{\mathbf{q}}{2} - \frac{\mathbf{k}}{\varepsilon}\right) \hat{u}_\varepsilon^*\left(\frac{\mathbf{q}}{2} + \frac{\mathbf{k}}{\varepsilon}\right) \\ &= \frac{\varepsilon}{(2\pi)^d} \frac{|\hat{\varphi}(\mathbf{k})|^2}{[i\varepsilon\alpha + \frac{\omega^2}{c_0^2} - |\mathbf{k} + \frac{\varepsilon\mathbf{q}}{2}|^2][-i\varepsilon\alpha + \frac{\omega^2}{c_0^2} - |\mathbf{k} - \frac{\varepsilon\mathbf{q}}{2}|^2]} + l.o.t. \\ &= \frac{\varepsilon}{(2\pi)^d} \frac{|\hat{\varphi}(\mathbf{k})|^2}{\left(\frac{\omega^2}{c_0^2} - |\mathbf{k}|^2\right)^2 - (i\varepsilon\alpha - \varepsilon\mathbf{k} \cdot \mathbf{q})^2} + l.o.t. \\ &= \frac{\varepsilon}{(2\pi)^d} \frac{|\hat{\varphi}(\mathbf{k})|^2}{2i\varepsilon\alpha - 2\varepsilon\mathbf{k} \cdot \mathbf{q}} \left[\frac{1}{\left(\frac{\omega^2}{c_0^2} - |\mathbf{k}|^2\right) - i\varepsilon\alpha} - \frac{1}{\left(\frac{\omega^2}{c_0^2} - |\mathbf{k}|^2\right) + i\varepsilon\alpha} \right] + l.o.t. \\ &= \frac{1}{i(2\pi)^d} \frac{|\hat{\varphi}(\mathbf{k})|^2}{2\alpha + i2\mathbf{k} \cdot \mathbf{q}} 2\pi i \delta\left(\frac{\omega^2}{c_0^2} - |\mathbf{k}|^2\right) + l.o.t. \\ &= \frac{1}{2\alpha + i2\mathbf{k} \cdot \mathbf{q}} \frac{|\hat{\varphi}(\mathbf{k})|^2}{(2\pi)^{d-1}} \delta\left(\frac{\omega^2}{c_0^2} - |\mathbf{k}|^2\right) + l.o.t. \end{aligned}$$

Here, *l.o.t.* refers to terms that tend to 0 in the sense of distributions as $\varepsilon \rightarrow 0$. We refer the reader to e.g. [15] for a more rigorous derivation. This shows that in the limit $\varepsilon \rightarrow 0$, we have

$$(2\alpha + i2\mathbf{k} \cdot \mathbf{q}) \hat{W}(\mathbf{q}, \mathbf{k}) = \frac{|\hat{\varphi}(\mathbf{k})|^2}{(2\pi)^{d-1}} \delta\left(\frac{\omega^2}{c_0^2} - |\mathbf{k}|^2\right).$$

Sending the regularizing parameters $\alpha \rightarrow 0^+$ and denoting by $a(\mathbf{x}, \mathbf{k})$ the inverse Fourier transform $\mathbf{q} \rightarrow \mathbf{x}$ of \hat{W} , we obtain the Liouville equation (19).

In the presence of scatterers whose density vanishes at $\mathbf{x} = \mathbf{x}_0$, the radiating source term $Q(\mathbf{x}, \mathbf{k})$ is not modified and propagation in a homogeneous medium is replaced formally by propagation in a scattering medium as in the preceding section. The phase-space energy density $a(\mathbf{x}, \mathbf{k})$ thus solves the following stationary transport equation

$$c_0 \hat{\mathbf{k}} \cdot \nabla a + \Sigma(\mathbf{x}, \mathbf{k}) a = \int_{\mathbb{R}^d} \sigma(\mathbf{x}, \mathbf{k}, \mathbf{q}) a(\mathbf{x}, \mathbf{q}) \delta(c_0|\mathbf{k}| - c_0|\mathbf{q}|) d\mathbf{q} + Q(\mathbf{x}, \mathbf{k}). \quad (21)$$

The equation should be augmented with zero-incoming radiation conditions, i.e., $a(\mathbf{x} - t\mathbf{k}, \mathbf{k}) \rightarrow 0$ as $t \rightarrow +\infty$. In practice, we choose the source term $\varphi(\mathbf{x}) = \delta(\mathbf{x})$ so that $\hat{\varphi}(\mathbf{k}) = 1$.

2.3 Foldy-Lax model for point scatterers

The Helmholtz equation (17) is very demanding to solve numerically for the choice of sound speed fluctuations given in (5). Since $\beta > 0$ so that $\varepsilon^\beta \rightarrow 0$ as $\varepsilon \rightarrow 0$, the localized scatterers are very small compared to the wavelength of the propagating waves. As a consequence, we can replace the localized scatterers by point scatterers. We thus have to solve a Helmholtz equation with randomly distributed point scatterers.

Assuming that the number of scatterers on a given computational domain is N , we obtain that the solution to the Helmholtz equation is given by

$$u(\mathbf{x}) = u^i(\mathbf{x}) + \sum_{j=1}^N \tau_j G_0(\mathbf{x}, \mathbf{x}_j) u(\mathbf{x}_j), \quad (22)$$

where $u^i(\mathbf{x})$ is the wave field generated by the source and the Green's function $G_0(\mathbf{x}, \mathbf{x}')$ is given by

$$G_0(\mathbf{x}, \mathbf{x}') = \begin{cases} \frac{i}{4} H_0^1(k|\mathbf{x} - \mathbf{x}'|), & d = 2, \\ \frac{e^{ik|\mathbf{x} - \mathbf{x}'|}}{4\pi|\mathbf{x} - \mathbf{x}'|}, & d = 3, \end{cases} \quad (23)$$

with H_0^1 the 0th order Hankel function of the first kind. When $\mathbf{x} = \mathbf{x}_j$, the above solution needs modification. The Foldy-Lax model [23, 27, 38] removes the singularities in a self-consistent fashion by imposing that

$$u(\mathbf{x}_j) = u^i(\mathbf{x}_j) + \sum_{\substack{j'=1 \\ j' \neq j}}^N \tau_{j'} G_0(\mathbf{x}_j; \mathbf{x}_{j'}) u(\mathbf{x}_{j'}), \quad (24)$$

for $j = 1, \dots, N$. We thus need to solve the system (24) first and then can evaluate the field $u(\mathbf{x})$ at each point \mathbf{x} using (22).

The Foldy-Lax equation (24) can be written in matrix form as:

$$\mathbf{H}\mathbf{U} = \mathbf{U}^i, \quad (25)$$

where

$$\mathbf{U} \equiv [u(\mathbf{x}_1), \dots, u(\mathbf{x}_N)]^T, \quad \mathbf{U}^i \equiv [u^i(\mathbf{x}_1), \dots, u^i(\mathbf{x}_N)]^T, \quad (26)$$

and where the complex matrix \mathbf{H} is given by

$$H_{jj'} = \delta_{jj'} - (1 - \delta_{jj'}) \tau_{j'} G_0(\mathbf{x}_j, \mathbf{x}_{j'}). \quad (27)$$

Let us assume to simplify that the strength of the scatterers is given by $\tau_j = \epsilon_j \tau k^2$, where the ϵ_j are independent variables taking the values 1 and -1 with equal probability. This is the setting that we will consider in the next section. We then verify that

$$\Sigma_{2D}(\mathbf{x}) = \frac{k^3 \tau^2 n_0}{4}, \quad \sigma_{2D}(\mathbf{x}, \mathbf{k}, \mathbf{k}') = \frac{k^3 \tau^2 n_0}{8\pi}, \quad (28)$$

in the two-dimensional case and

$$\Sigma_{3D}(\mathbf{x}) = \frac{k^4 \tau^2 n_0}{4\pi}, \quad \sigma_{3D}(\mathbf{x}, \mathbf{k}, \mathbf{k}') = \frac{k^4 \tau^2 n_0}{16\pi^2}, \quad (29)$$

in the three-dimensional case. These expressions are consistent with (14) provided that we set $L = 1$ and normalize the sound speed $c_0 = 1$. We shall assume that $L = 1$ and $c_0 = 1$ for the rest of the paper.

2.4 Models for the buried inclusions

We now have to model the buried inclusions, both at the level of the Helmholtz equation and of the radiative transfer equation.

The Foldy-Lax model can be generalized to account for the presence of extended objects. Here, we consider impenetrable objects with vanishing Neumann boundary conditions at the inclusion's boundary for the Helmholtz equation. In this setting, (22) becomes

$$u(\mathbf{x}) = u^i(\mathbf{x}, \mathbf{x}') + \sum_{j=1}^N \tau_j G_0(\mathbf{x}; \mathbf{x}_j) u(\mathbf{x}_j) + \sum_{l=1}^M \int_{\partial\Omega_l} \mathbf{n}_l \cdot \nabla_{\mathbf{y}} G_0(\mathbf{x}; \mathbf{y}) u(\mathbf{y}) dS(\mathbf{y}), \quad (30)$$

where M is the number of extended objects in the domain and Ω_l is the l -th inclusion with sufficiently smooth boundary $\partial\Omega_l$ and outer normal vector $-\mathbf{n}_l$ on the boundary. The Foldy-Lax consistent equation now becomes

$$u(\mathbf{x}_j) = u^i(\mathbf{x}_j) + \sum_{j' \neq j}^N \tau_{j'} G_0(\mathbf{x}_j; \mathbf{x}_{j'}) u(\mathbf{x}_{j'}) + \sum_{l=1}^M \int_{\partial\Omega_l} \mathbf{n}_l \cdot \nabla_{\mathbf{y}} G_0(\mathbf{x}_j; \mathbf{y}) u(\mathbf{y}) dS(\mathbf{y}), \quad (31)$$

for $j = 1, \dots, N$.

In order to evaluate wave fields at arbitrary points \mathbf{x} , we need to solve (30) for points on the boundary of the extended objects and (31) for $\mathbf{x}_j, j = 1, \dots, N$. Equations (30) and (31) are the new self-consistent Foldy-Lax multiple scattering equations in the case where extended objects are present.

At the transport level, in order to obtain a contribution of order $O(1)$, we need to assume that the inclusion is comparable in size to the overall distance of propagation. This implies that the extended object is large compared to the wavelength ε so that its boundary may be treated as specularly reflecting. In other words, we assume the following specular reflection:

$$a(\mathbf{x}, \mathbf{k}) = a(\mathbf{x}, \mathbf{k} - 2\mathbf{k} \cdot \mathbf{n}(\mathbf{x})\mathbf{n}(\mathbf{x})), \quad \mathbf{x} \in \partial\Omega_l. \quad (32)$$

The radiative transfer equation (21) holds outside of the inclusions, i.e., on $\mathbb{R}^d \setminus (\cup_l \Omega_l)$.

3 Numerical validations

Although radiative transfer equations have been used for a long time to describe the energy density of waves in random media, numerical validations of such models are more recent; see e.g. [8, 31] for simulations in the time domain. The reason is that the propagation of high frequency waves in highly heterogeneous media is computationally quite expensive. In this section, we compare the energy densities of monochromatic waves based on the Foldy Lax model with the solution of the corresponding radiative transfer equation.

3.1 The wave and transport solvers

The Foldy-Lax consistent equations (25) form a system of complex-valued algebraic equations. Because the matrix \mathbf{H} is dense, iterative methods are not more efficient

than direct solvers. We thus solve the system by the LU factorization method. In the case where extended objects are present in the domain, we need to solve (30) and (31). We approximate the boundary integrals by standard numerical quadrature rules. Since these integrals are weakly singular, we adopt the kernel splitting method developed in [20] to discretize the integrals.

The random medium is generated by distributing the random scatterers according to a Poisson point process of density n_0 . We recall that for a bounded volume element V , the number of points in V has the distribution $\mathbb{P}(N_V = k) = \frac{e^{-n_0|V|}(n_0|V|)^k}{k!}$ for $k \geq 0$, where $|V|$ is the (Lebesgue) measure of V . Once a realization of the number k is chosen, the k points are placed in V using a uniform (normalized Lebesgue) distribution on V . A typical distribution of point scatterers is shown in e.g. Fig. 1.

The transport equation (21) is solved by the Monte Carlo method [37]. We run enough particles to ensure that the statistical error in the simulation is smaller than any other involved quantity. Appropriate variance reduction techniques are used to calculate the influence of extended objects accurately; see [8] for the details.

Note that the Foldy-Lax model and the radiative transfer equations work for a given (large) frequency. By varying the frequency in a (small) vicinity of a central frequency, time-domain data may be obtained by appropriate Fourier transform.

3.2 Numerical results

To compare the wave and transport models, we compute the total energy on a fixed array of detectors D ; see Fig. 1. After appropriate normalization, the energies take the form:

$$E_W = \int_D |u(\mathbf{x})|^2 d\mathbf{x} \quad \text{and} \quad E_T = \int_D \int_{S^{d-1}} a(\mathbf{x}, \hat{\mathbf{k}}) d\hat{\mathbf{k}} d\mathbf{x}, \quad (33)$$

where $u(\mathbf{x})$ is the random solution to the wave equation and $a(\mathbf{x}, \hat{\mathbf{k}})$ is the energy density of those waves at position \mathbf{x} propagating in direction $\hat{\mathbf{k}} \in S^{d-1}$, where $d = 2$ in all our numerical simulations.

Since $u(\mathbf{x})$ is a random variable, E_W is also a random variable, which thus depends on the realization of the random medium. Note that E_T in contrast is a deterministic quantity. We have therefore two objectives: (i) show that $\mathbb{E}\{E_W\}$ is close to E_T ; and (ii) show that the standard deviation $\sigma(E_W)$ of E_W is small. The latter is defined as

$$\sigma(E_W) = \left(\mathbb{E}\{(E_W - \mathbb{E}\{E_W\})^2\} \right)^{\frac{1}{2}}. \quad (34)$$

From now on, we use the standard notation σ to denote standard deviations, which should not be confused with the scattering cross-section in (21). We are interested in the behavior of $\sigma(E_W)$ as a function of the mean free path $c_0 \Sigma^{-1}$.

Energy measurements and detector size. The first numerical test compares wave and transport data in the absence of any buried inclusion. The setup is as shown in Fig. 1. We compare the models for five frequencies uniformly distributed on $[\omega \ 1.25\omega]$, where $\omega = \frac{2\pi}{\lambda}$. The domain of interest is fixed and given by $[0 \ 400\lambda] \times [0 \ 200\lambda]$. The point source is located at position $(220\lambda, -40\lambda)$. A total number of 6000 point scatterers on average (using a Poisson distribution) are randomly distributed in the domain. This

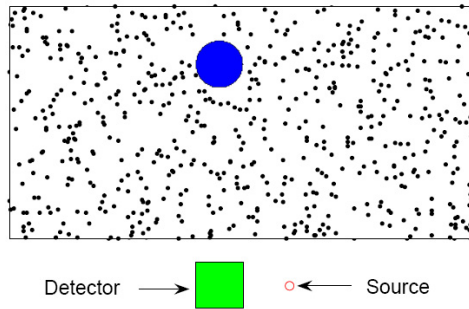


Figure 1: Setup for the numerical simulations. The inclusion may be placed inside or outside of the random medium. We show here a typical realization of the distribution of 1000 point scatterers.

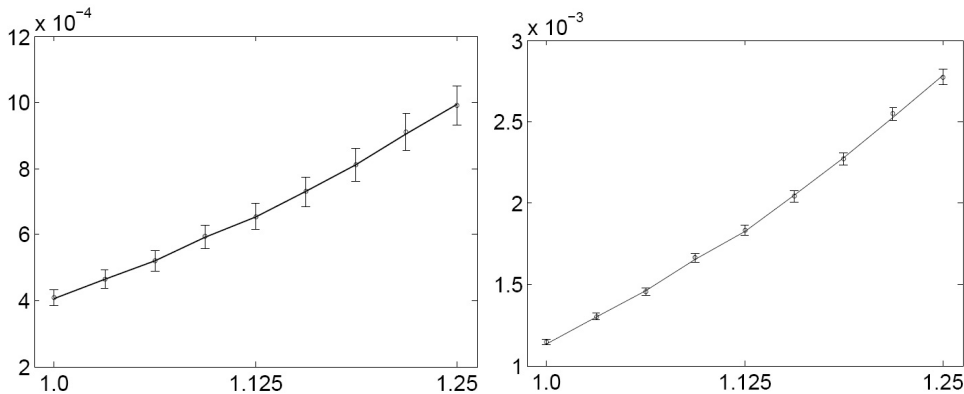


Figure 2: Comparison between measured transport and wave data at frequencies between $\omega = \frac{2\pi}{\lambda}$ and 1.25ω with detectors of size $40\lambda \times 40\lambda$ (left) and $80\lambda \times 80\lambda$ (right), respectively. Solid line: transport data E_T ; Circles with error bar: wave data $\mathbb{E}\{E_W\}$ and its standard deviation $\sigma(E_W)$.

corresponds to a correlation length $l_c \approx 3.65\lambda$. The strength of the scatterers is chosen such that the mean free path is equal to 40λ . As the frequency increases, the transport mean free path decreases as the third power of frequency as can be seen in (28). We show in Fig. 2 a comparison between E_W and E_T at different frequencies with two different sizes of the array of detectors. The average $\mathbb{E}\{E_W\}$ and standard deviation $\sigma(E_w)$ are calculated based on 40 realizations of the random medium.

We observe that the wave and transport models agree quite well. The ensemble average of the energy density is well captured by the radiative transfer equation. However, radiative transfer models are valid when energy is averaged over a sufficiently large domain compared to the wavelength [4, 6]. When averaging takes place over too small a detector, statistical instabilities are important.

These results generalize to the case where an inclusion is present in the random medium. The comparison between the energy densities E_W and E_T is then qualitatively very similar to the case shown in Fig. 2.

Statistical stability and density of scatterers. In the next numerical example, we want to address the statistical stability of the transport model with respect to the

number of random scatterers. The same average scattering medium, characterized by a given mean free path, may be obtained from a low density of strong scatterers or a high density of weak scatterers in such a way that $\tau^2 n_0$ stays constant. We do not have a theoretical model at present to characterize the statistical stability of the energy E_W when τ and n_0 vary while the product $\tau^2 n_0$ remains constant. Intuitively however, we expect the random medium to be more mixing and thus more stable statistically when the number of scatterers is large simply because the interactions of the wave fields with the underlying structure happen more often. The following numerical simulations confirm this. We show in Fig. 3 the energy measurements obtained from nine types

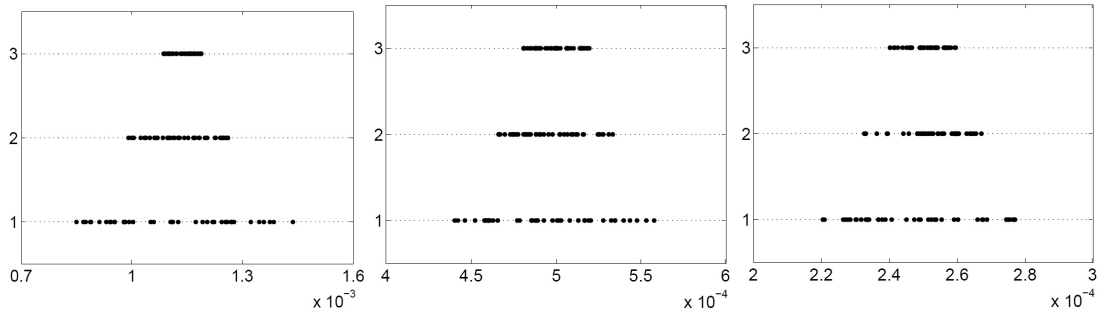


Figure 3: Statistical stability of wave data with respect to media properties at two mean free paths: $c_0 \Sigma^{-1} = 30\lambda$ (left), $c_0 \Sigma^{-1} = 50\lambda$ (middle) and $c_0 \Sigma^{-1} = 100\lambda$ (right). Each dot corresponds to the wave energy measured on the array of detectors for one realization with an average of 6000 scatterers (top lines labeled 3; $l_c \approx 3.65\lambda$), 3000 scatterers (middle lines labeled 2; $l_c \approx 5.16\lambda$), and 1500 scatterers (bottom lines labeled 1; $l_c \approx 7.30\lambda$), respectively.

of random media corresponding to an average of 6000 scatterers ($l_c \approx 3.65\lambda$), 3000 scatterers ($l_c \approx 5.16\lambda$), and 1500 scatterers ($l_c \approx 7.30\lambda$), and to mean free paths $c_0 \Sigma^{-1}$ equal to 30λ , 50λ , and 100λ . We observe as expected that the standard deviation increases with the correlation length in the medium (as statistical instability increases) and that it increases when the mean free path decreases (as the random medium becomes optically thicker); see the statistics in Tab. 1.

	$c_0 \Sigma^{-1} = 30\lambda$			$c_0 \Sigma^{-1} = 50\lambda$			$c_0 \Sigma^{-1} = 100\lambda$		
	6000	3000	1500	6000	3000	1500	6000	3000	1500
$\mathbb{E}\{E_W\} \times 10^3$	1.145	1.150	1.150	0.500	0.496	0.495	0.251	0.253	0.249
$\sigma(E_W) \times 10^4$	0.425	0.711	1.156	0.123	0.204	0.383	0.055	0.093	0.181
$\frac{\sigma(E_W)}{\mathbb{E}\{E_W\}} \times 10^2$	3.71	6.18	10.05	2.46	4.11	7.73	2.19	3.69	7.27

Table 1: Average and standard deviation of the wave energy measurements presented in Fig. 3.

4 Transport-based imaging in random media

We now examine the capabilities of the radiative transfer model to detect and image inclusions buried in random media. As in the preceding section, all simulations are

performed in a two-dimensional setting, which is appropriate for the experimental configuration considered in e.g. [29]. Note that both the Foldy-Lax model and the Monte Carlo method are independent of dimension so the proposed numerical method is essentially independent of spatial dimension.

As we saw in Section 2, the wave energy density is modeled by a radiative transfer equation given by (21) outside of the buried inclusions and by specular reflection conditions (32) at the inclusions' boundary. The inclusions thus become constitutive parameters in the radiative transfer equation, as is the mean free path $c_0\Sigma^{-1}(\mathbf{x})$. In this section, we propose to reconstruct the mean free path and the inclusion in (21)-(32) using energy measurements obtained by solving the Foldy-Lax equation (22)-(24). Although inverse transport models have been used already, see e.g. [1, 32], this is to our knowledge the first analysis of reconstructions based on a macroscopic (wavelength-independent) transport model from microscopic (wave- and medium-dependent) wave data.

We consider three slightly different settings: inclusions buried inside a random medium; inclusions separated from the array of detectors by a random medium; and inclusion buried in a random medium and located behind a large blocker that prevents direct line of sight from the source location. The settings are shown in Fig. 4.

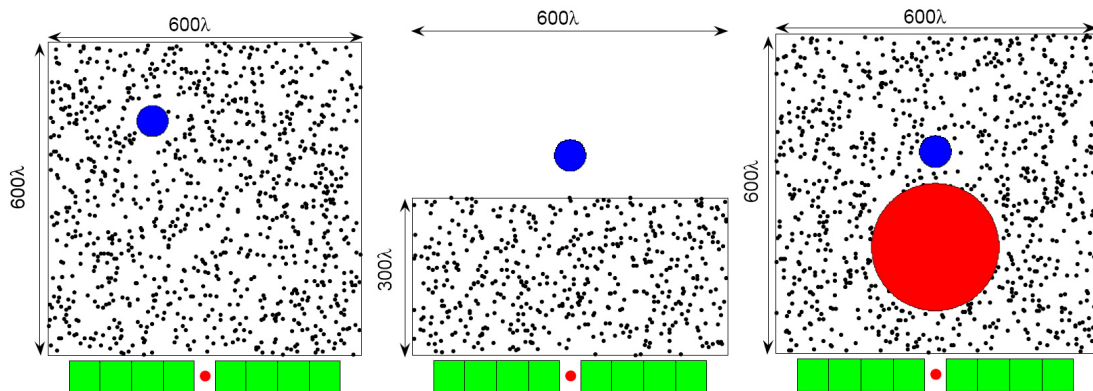


Figure 4: Three different setups for the reconstructions: inclusion inside the medium (left), inclusion outside of the medium (middle), and inclusion behind a blocker (right). The small circles and (green) squares represent the source and detector locations, respectively. The small (blue) disks are the inclusions to be reconstructed. The large (red) disk represents a blocker, whose location and geometry is assumed to be known.

The theory of inverse problems for transport equations is relatively well established in the presence of phase-space measurements; see [18]. Here however, we assume that E_W and E_T are available, not $a(\mathbf{x}, \hat{\mathbf{k}})$ for all $\mathbf{x} \in D$ and $\hat{\mathbf{k}} \in S^{d-1}$. As a consequence, and even though no rigorous theoretical results exist in this domain, the measurements we have are similar to partial knowledge of the Cauchy data in an inverse elliptic problem [24]. The stability of such inverse problems is notoriously bad, in the sense that noise is drastically amplified during the inversion. What this means in practice is that the number of degrees of freedom about the random medium and the inclusion that we can possibly retrieve from available data is *small*. The inverse transport problem thus needs to be parameterized. Our choice of a parameterization is the following: we assume that the mean free path $c_0\Sigma^{-1}$ is constant in a rectangular domain whose geometry is

known, and vanishes outside of that domain; and we assume that the inclusion is a disc parameterized by its location \mathbf{x} and its radius R . This hypothesis is slightly relaxed in Section 4.3.

4.1 Transport-based imaging method

The reconstruction method for the parameters mentioned above is based on the following least-square minimization procedure. Let \mathcal{F} be the family of parameters we want to reconstruct. We find these parameters by solving the following minimization problem:

$$\mathcal{F}_b = \arg \min_{\mathcal{F} \in \Xi} \mathcal{O}(\mathcal{F}), \quad (35)$$

where $\Xi = [\mathcal{F}_{min}, \mathcal{F}_{max}]$ is a family of a priori box-constraints that define a region in which we search for optimal solutions. The objective function that measures the mismatch between measured data and model prediction is given by:

$$\mathcal{O}(\mathcal{F}) = \frac{1}{2} \sum_{j=1}^J |E_T^j - E_W^j|^2, \quad (36)$$

where E_T^j is the model prediction on detector j , E_W^j the corresponding wave measurement, and J the total number of detectors. We solve this minimization problem by a quasi-Newton minimization algorithm with BFGS updating rules for the Hessian matrix. Box constraints on decision variables are enforced by a gradient projection method. The gradient of the objective function with respect to the parameters to be recovered is calculated by using a finite difference approximation since we have only a few parameters to reconstruct. We refer the interested reader to [14, 30] for details on the BFGS quasi-Newton method and [32] for application of the method in inverse transport problems.

In all of the inversions run below, we consider 8 detectors of size $62.5\lambda \times 80\lambda$, as is depicted in Fig. 4. We have mentioned that the energy density was statistically stable only on sufficiently large domains. The size of the detectors thus needs to be sufficiently large to average over local fluctuations. The number of detectors also needs to be sufficiently large to increase the amount of available data. We do not possess a theory for the energy-energy correlations that could guide us in the design of optimal detectors array. Several scenarios have been tested and the number of 8 detectors is optimal in terms of the statistical stability and the amount of non-redundant information it provides.

The box-constraints Ξ have also been chosen to be fairly non-constraining. For an inclusion of radius $R = 30\lambda$ and location $(300\lambda, 400\lambda)$ in a random medium of size $[0 \ 600\lambda] \times [0 \ 600\lambda]$ for instance, the constraints on the radius are $R \in [10\lambda, 100\lambda]$ and the constraints on the locations (x, y) are $[50\lambda \ 550\lambda] \times [50\lambda \ 550\lambda]$.

4.2 Imaging under different measurement scenarios

We consider two imaging scenarios: (i) when we have wave energy measurements in the presence of the object; and (ii) when we have energy measurements in the presence *and* in the absence of the inclusion. The former measurements are referred to as *direct* measurements. The latter measurements are referred to as *differential* measurements.

4.2.1 Scenario I: direct measurement

In this first scenario, we are not able to probe the random medium in the absence of an inclusion. We distinguish two sub-scenarios, which essentially have the same reconstruction capabilities. In Scenario Ia, we assume that we have access to measurements in the absence of the inclusion for a given realization of the random medium, which we call medium 1. We then assume that we have access to measurements in the presence of the inclusion in a medium 2 that is completely uncorrelated to medium 1. In scenario Ib, we assume that we have access to the measurements in medium 2 only, whence in the presence of the inclusion. The difference is mostly pedagogical. In scenario Ia, we first reconstruct the parameters of the random medium, i.e., here the mean free path $c_0\Sigma^{-1}$, and second reconstruct the inclusions' parameters. In scenario Ib, we have to reconstruct all parameters at once. We show numerical evidence that both scenarios provide very similar reconstruction capabilities. In both cases, the inclusion's influence on the measurements needs to be greater than the noise level coming from our lack of understanding of the specific realization of the random medium. In other words, the inclusion's influence need be larger than the statistical instability of the radiative transfer model. The reconstruction in scenario Ia is a two step process:

Step A. We measure the energy density of waves propagating in one realization of the random medium described above. We then estimate the scattering cross-section Σ by solving the following minimization problem:

$$\Sigma_b = \arg \min_{\Sigma \in \Xi_A} \mathcal{O}(\Sigma), \quad (37)$$

where $\Xi_A = [\Sigma_{min}, \Sigma_{max}]$ is the space in which we seek Σ , and the objective functional is given by

$$\mathcal{O}(\Sigma) = \frac{1}{2} \sum_{j=1}^J |E_T^j - E_W^j|^2, \quad (38)$$

where E_T^j is the model prediction detector j , and E_W^j is the corresponding wave energy measurement.

Step B. We now perform the energy measurements in the presence of an inclusion buried in a medium 2 uncorrelated with the medium used in Step A. Such a scenario is realistic when we know that medium 2 has similar statistics to medium 1, on which more refined estimates can be obtained before measurements in medium 2 are performed.

We use the scattering coefficient Σ_b (b for best fit) obtained in Step A and image the inclusion from available measurements in medium 2. The position and radius of the inclusion, assumed to be a disc, are obtained by the following minimization:

$$(\mathbf{x}_b, R_b) = \arg \min_{(\mathbf{x}, R) \in \Xi_B} \mathcal{O}(\mathbf{x}, R). \quad (39)$$

Here $\mathcal{O}(\mathbf{x}, R)$ is defined as in (36) with E_T^j the transport solutions with scattering cross-section Σ_b and E_W^j the wave energy measurements in medium 2. Here, $\Xi_B \subset \mathbb{R}^{d+1}$ is the constraint set in which the solution (\mathbf{x}, R) is looked for.

We show in Fig. 5 four typical reconstructions ((A)-(D) from left to right) with this two-step procedure. The reconstructions in (A) and (B) are done for the first configuration in Fig. 4 where the medium covers the domain $[0 \ 600\lambda] \times [0 \ 600\lambda]$ and

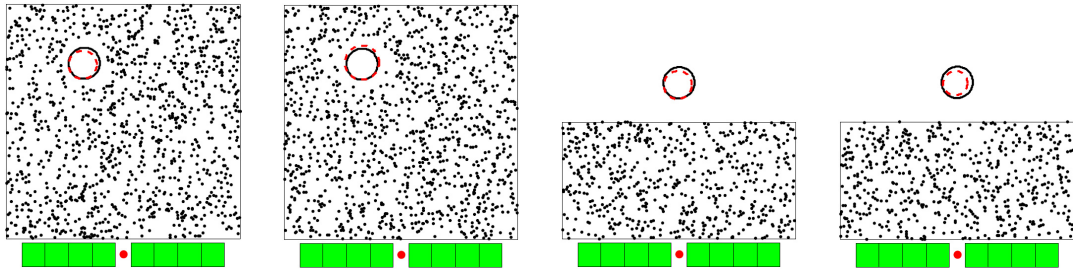


Figure 5: Typical reconstruction of an inclusion from direct measurements under Scenario Ia. (A) and (C) are for $c_0 \Sigma^{-1} = 200\lambda$. (B) and (D) are for $c_0 \Sigma^{-1} = 100\lambda$. Real and reconstructed objects are plotted as solid and dotted circles, respectively.

the inclusion is located inside the medium. A few scatterers around the inclusions are removed from the picture to make the plot clearer. The reconstructions in (C) and (D) are done for the second configuration in Fig. 4 where the medium covers the domain $[0, 600\lambda] \times [0, 300\lambda]$ and the inclusion is located outside of the medium. The mean free path (with $c_0 = 1$) for the medium in (A) and (C) is $c_0 \Sigma^{-1} = 200\lambda$ and that for the medium in (B) and (D) is $c_0 \Sigma^{-1} = 100\lambda$. In all experiments, the correlation length is $l_c \approx 7.75\lambda$, with an average of 6000 rods in experiments (A)&(C) and of 3000 rods in experiments (B)&(D).

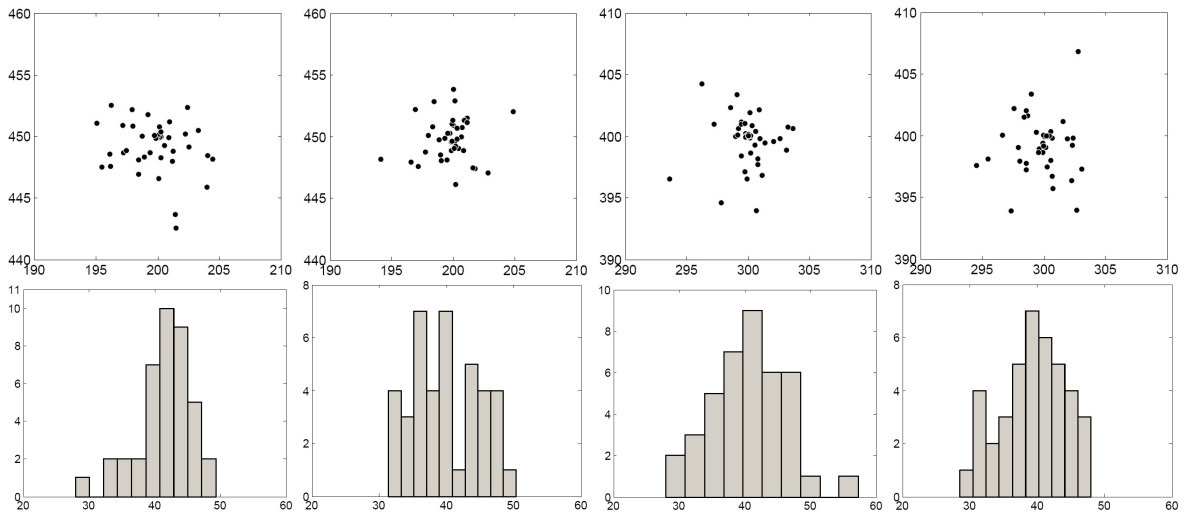


Figure 6: Reconstructed parameters for the four cases in Fig. 5 based on 40 realizations. Top row: distribution of the reconstructed inclusion's locations. Bottom row: histogram of the reconstructed radii.

The reconstructions are repeated for 40 different realizations of the random medium. The results are presented in Fig. 6, where we have plotted the reconstructed locations and radii for the four cases shown in Fig. 5. We observe that in all cases, the reconstructions of the inclusion's location are quite accurate. The radii are also good, though not as accurate. Given the smallness (relative to the mean free path) of the inclusions, we do not expect to reconstruct their size very precisely.

We have calculated the first two statistical moments (expectation and standard deviation) of the mean free path, the inclusions' locations (measured by x - and y - coordinates).

dinates), and the inclusions' radii. The numbers are presented in Tab. 2. We observe that the reconstruction of the inclusion's location is relatively good, as the variance is quite small. The error in the reconstruction of the inclusion's geometry is however significantly larger.

	Inclusion			Reconstruction ^a		
	$c_0\Sigma^{-1}$	location	R	$c_0\Sigma_b^{-1}$	location	R
Case A	200	(200, 450)	40	200.0 [2.7]	(199.8 [2.4], 449.2 [2.1])	41.5 [4.3]
Case B	100	(200, 450)	40	99.8 [2.7]	(199.8 [1.8], 449.8 [1.7])	40.0 [5.1]
Case C	200	(300, 400)	40	200.6 [3.3]	(300.0 [1.8], 399.7 [2.1])	40.4 [6.0]
Case D	100	(300, 400)	40	100.1 [2.9]	(299.8 [1.9], 399.2 [2.4])	39.3 [4.9]

Table 2: Reconstructed mean free paths, locations and radii from the four cases in Fig. 5. All numbers are in units of the wavelength λ . ^aAveraged value and standard deviation (numbers in bracket) calculated from 40 realizations.

Another way of looking at the instability in the reconstruction is to plot the functional that appears in the minimization problem in the vicinity of the minimum. We plot in Fig. 7 (left) the functional for different values of x in the vicinity of $x = x_{\min}$ at y and R fixed and equal to their optimal values. Similarly, the middle plot shows the functional as a function of y at x and R fixed and the right plot the functional as a function of R at (x, y) fixed. The results presented in Fig. 7 for a specific real-

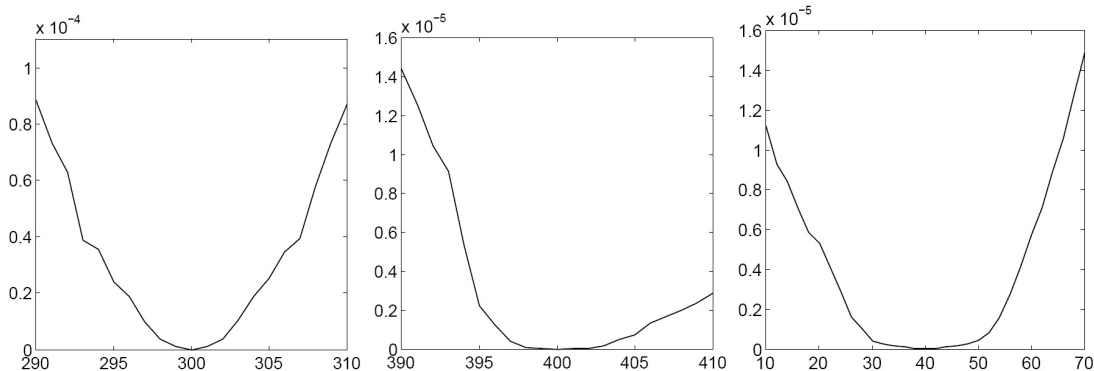


Figure 7: Plot of the objective function $\mathcal{O}(\mathbf{x})$ as a function of x (left) at y and R fixed, as a function of y (middle) at x and R fixed and as a function of R (right) at (x, y) fixed, for a typical realization of the random medium.

ization show a sharper resolution in the x (cross-range) variable than in the y (range) variable. This may be explained by the fact that the detectors have a wide aperture in the x variable and much less aperture in the y variable. The results presented in Tab. 2, however, show that the standard deviations in the x and y variables are somewhat comparable (and on the order of $2 - 3\lambda$, less than 1% of the distance from the source to the inclusion). This is an indication that the regime of wave propagation is quite highly mixing so that there is no real privileged direction of propagation.

As we have mentioned in Section 3, the statistical stability of the wave energy measurements depends on the number of scatterers for a given mean free path. We now

consider the reconstruction of inclusions for two random media with a mean free path equal to $c_0\Sigma^{-1} = 100\lambda$. The first random medium has an average of 6000 point scatterers ($l_c \approx 7.75\lambda$) and the second random medium an average of 3000 point scatterers ($l_c \approx 10.95\lambda$). The results are presented in Fig. 8. We have also calculated the two

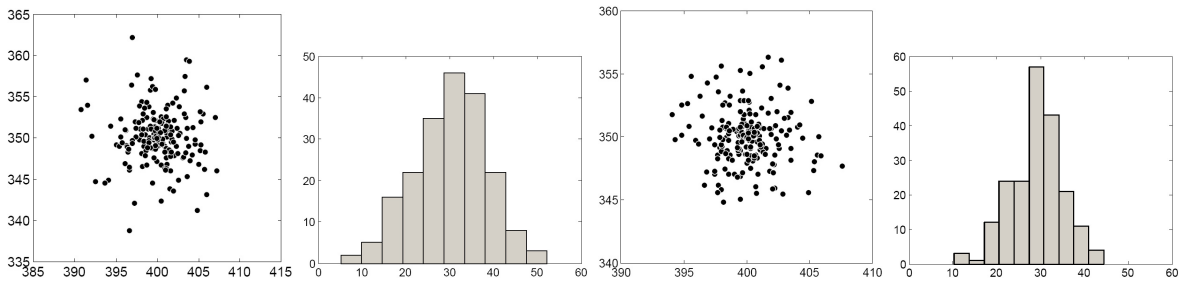


Figure 8: Distributions of the reconstructed locations and radii for 200 realizations of random media consisting of $N = 3000$ (left two plots) and $N = 6000$ (right two plots) point scatterers on average.

first statistical moments of the inclusions' location and radius. Results are reported in Tab. 3. The averaged values are very similar for both reconstructions, which is expected

	Inclusion			Reconstruction ^a		
	$c_0\Sigma^{-1}$	location	R	$c_0\Sigma_b^{-1}$	location	R
$N = 3000$	100	(400, 350)	30	99.8 [4.4]	(400.0 [2.9], 350.2 [3.2])	30.1 [8.4]
$N = 6000$	100	(400, 350)	30	100.0 [2.9]	(400.0 [2.2], 350.0 [2.2])	29.0 [5.9]

Table 3: Reconstructed mean free path, location and radius from media with $N = 3000$ and $N = 6000$ point scatterers on average. ^aAveraged value and standard deviation (numbers in bracket) calculated with 200 realizations. All numbers are in units of the wavelength λ .

since radiative transfer is indeed valid for the ensemble averaged energy density. The standard deviation however increases when the scatterers become fewer and stronger. In that case, our lack of understanding of the specific realization of the random medium creates large noise in the data, whence in the reconstructions. Such results are consistent with our numerical analysis of the statistical instability done in Section 3.

Let us conclude this section by a remark on the resolution of the method. With random media with 6000 scatterers on average and a mean free path of $c_0\Sigma^{-1} = 100\lambda$ on a square domain of size 600λ and an inclusion buried 375λ north of the source, we have good reconstructions for radii larger than 20λ . At about 20λ , the “optimal” radius obtained by minimization has a large probability of hitting the box constraints imposed on the radius and is thus meaningless. In the same configuration with a random medium with 3000 scatterers on average, the smallest radius we can confidently reconstruct increases to $R = 30$. These results lead to the following conclusion. Even in the presence of a highly mixing random medium (with 6000 scatterers, which may be large for most practical situations [29]), the inclusion needs to be quite large compared to the wavelength in order for its influence to be larger than the statistical instability of the wave energy measurements. In such a context, the only solution to better resolution is to have access to the measurements of Scenario II considered below.

4.2.2 Scenario Ib: reconstructing all at once

We now consider the setting where Σ and the inclusion's parameters are reconstructed in a single step because we do not possess any a priori knowledge of the statistics of the random medium. Compared to scenario Ib, we have one more parameter to reconstruct, and possibly many more parameters when the power spectrum is spatially dependent. However, the reconstruction of these parameters is more adapted to the random medium 2 than in Scenario Ia. Reconstructions are based on minimizing the functional:

$$(\Sigma_b, \mathbf{x}_b, R_b) = \arg \min_{(\Sigma, \mathbf{x}, R) \in \Xi} \mathcal{O}(\Sigma, \mathbf{x}, R), \quad (40)$$

where $\Xi \subset \mathbb{R}^3$ is a set of constraints.

This scenario is of equivalent complexity to the previous one since only one additional parameter is added. Moreover, so long as the inclusion is relatively small compared to the size of the domain, it will not affect the reconstruction of Σ in any significant way.

We show in Fig. 9 the same reconstructions under scenario Ib as those obtained under scenario Ia in Fig. 5 (A) and (B). The first two statistical moments of the reconstructed

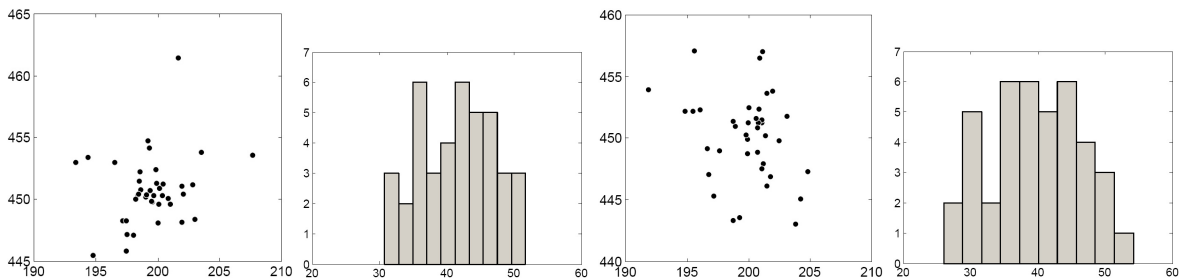


Figure 9: Distribution of reconstructed locations and radii with the method in Scenario Ib. Plots (A) and (B): for a medium with mean free path $c_0\Sigma^{-1} = 200\lambda$. Plots (C) and (D): for a medium with $c_0\Sigma^{-1} = 100\lambda$.

locations and radii are listed in Tab. 4. We observe that the reconstructed mean free paths, inclusion's positions and radii are very similar to the parameters reconstructed in Fig. 5.

	Inclusion			Reconstruction ^a		
	$c_0\Sigma^{-1}$	location	R	$c_0\Sigma_b^{-1}$	location	R
Medium 1	200	(200, 450)	40	200.6 [3.1]	(199.5 [2.6], 450.7 [2.8])	41.5 [5.7]
Medium 2	100	(200, 450)	40	99.0 [5.0]	(199.5 [3.4], 450.1 [3.5])	39.7 [7.0]

Table 4: Reconstructed mean free path, location and radius in Scenario Ib for two different type of media. ^aAveraged value and standard deviation (numbers in bracket) calculated from 40 realizations. All numbers are in units of the wavelength λ .

4.2.3 Scenario II: differential measurement

Scenario II relies on much different measurements. We assume that we have access to wave energy measurements in the presence and in the absence of the inclusion, and in

both cases for the *same* realization of the random medium (except at the location of the inclusion where the random scatterers are suppressed). However, we do not know the random medium and thus have to model it macroscopically using a radiative transfer model. As in the preceding case, the macroscopic model is parameterized by a unique parameter, the mean free path $c_0\Sigma^{-1}$.

As we said earlier, differential measurements allow for much more accurate reconstructions. The reason is that the difference of the two measured energies depends only on the inclusion. Therefore, with a kinematic picture in mind, where wave energy packets are replaced by particles scattering in the random media, all the wave packets that do not interact with the inclusion do not contribute to differential measurements. These wave packets are the largest contributors to the statistical instability of the random medium that hampers reconstructions of small objects in Scenario I. The measured wave packets that have interacted with the inclusion are also statistically unstable. However, they are in some sense proportional to the inclusion, and in the absence of external measurement noise, differential measurements allow one to reconstruct arbitrarily small objects. They are not immune to the statistical instability, and a statistical instability in the random medium of 10% may result in an error on the location and radius of the inclusion on the order of 10% as well. However, the limit in the size of the objects that can be reconstructed is governed by external measurement noise, and no longer by the statistical instability in the medium. The two-step reconstruction process used in scenario Ia applies here:

Step A. We use the measurements in the absence of an inclusion in the medium to estimate the scattering cross-section of the medium. This is done by minimizing (37) as before.

Step B. Once Σ has been found, we reconstruct the location (\mathbf{x}) and the radius (R) of the spherical inclusion by minimizing:

$$(\mathbf{x}_b, R_b) = \arg \min_{(\mathbf{x}, R) \in \Xi_B} \delta\mathcal{O}(\mathbf{x}, R) \quad (41)$$

where

$$\delta\mathcal{O}(\mathbf{x}, R) = \frac{1}{2} \sum_{j=1}^J |\delta E_T^j - \delta E_W^j|^2. \quad (42)$$

Here, δE_T^j and δE_W^j correspond to the difference of energies with and without the inclusion for the transport model and the wave data, respectively, at detector j . In practice, δE_W is calculated by estimating the difference of the solutions to two Foldy-Lax equations and δE_T is estimated by Monte Carlo using the variance reduction technique introduced in [8]. The role of this variance reduction is to write the difference δE_W as the expectation of an appropriate process, rather than the difference of two expectations, which requires a huge amount of particles to be accurate. We refer the reader to [8] for additional details.

Reconstructions based on Scenario II have been performed for two different mean free paths $c_0\Sigma^{-1} = 200\lambda$ and $c_0\Sigma^{-1} = 100\lambda$, respectively. The random medium is again formed of an average of 6000 scatterers over $[0, 600\lambda] \times [0, 600\lambda]$ so that the correlation length $l_c \approx 7.75\lambda$. The inclusion is located at coordinate $(375\lambda, 375\lambda)$ and has a radius equal to $R = 10\lambda$, which is significantly smaller than what we can reconstruct under scenario I.

We show in Fig. 10 the distributions of the reconstructed locations and radii for the two random media.

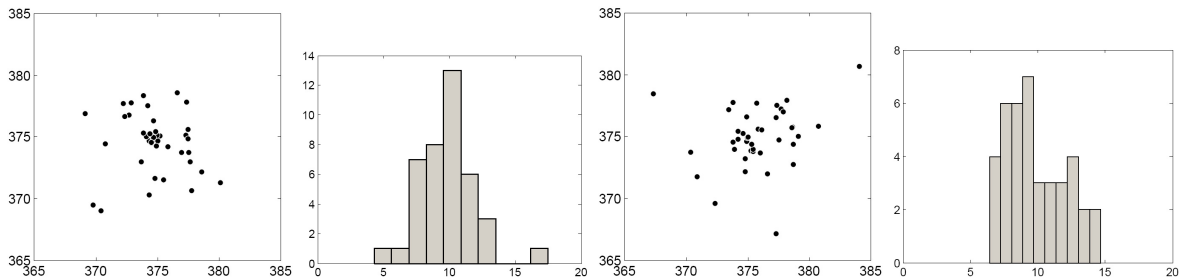


Figure 10: Distribution of reconstructed location and radius for 40 realizations with differential measurement. Left: $c_0 \Sigma^{-1} = 200\lambda$ and Right: $c_0 \Sigma^{-1} = 100\lambda$.

	Real			Reconstruction ^a		
	$c_0 \Sigma^{-1}$	location	R	$c_0 \Sigma_b^{-1}$	location	R
Medium 1	200	(375, 375)	10	199.8 [2.8]	(374.8 [2.4], 374.6 [2.4])	9.9 [2.3]
Medium 2	100	(375, 375)	10	100.1 [3.3]	(375.8 [2.9], 375.0 [2.4])	9.9 [2.2]

Table 5: Reconstructed mean free paths, locations and radii based on differential measurements. ^aAveraged value and standard deviation (numbers in bracket) calculated from 40 realizations. All numbers are in units of the wavelength λ .

The averaged value and standard deviation of the mean free path and the inclusion's location and radius are summarized in Tab. 5. As we can observe, the transport inversion does a relatively good job at locating the inclusion. However, it misses the size of the inclusion by a much larger amount. This is understandable because the specular reflection model may not be totally consistent with the size of an object with radius of order 10λ . For smaller objects, a more accurate radiation model than specular reflection is necessary. We do not consider this issue further here.

4.3 Imaging the orientation of the inclusions

In the preceding sections, we have obtained satisfactory reconstructions of inclusions based on low-dimensional parameterizations of the inclusion. Since, as we have mentioned in Section 4, the inverse transport problem is quite ill-posed, we should not expect to reconstruct any fine geometrical information about the inclusion. To demonstrate this, we consider the reconstruction of half discs from wave energy measurements. Half discs are parameterized by their location, their radius, and the orientation θ of their flat portion (with respect to the x -axis). We use the same minimization techniques as in the preceding sections with this additional parameter θ in the functional in (36) in the case of direct measurements and (42) in the case of differential measurements.

We show in Fig. 11 typical reconstructions obtained from direct and differential measurement. The radius of the inclusion is $R = 30\lambda$ for the case of differential measurement and $R = 50\lambda$ for the case of direct measurement. In both cases, the half disc is centered at position $(375\lambda, 375\lambda)$. The reconstruction of the orientation is relatively accurate.

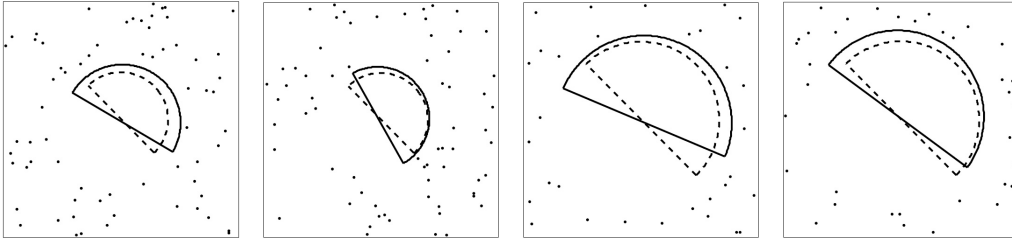


Figure 11: Reconstructions of half discs from direct and differential measurements in random media with an average of 6000 scatterers and a mean free path $c_0\Sigma^{-1} = 100\lambda$. From left to right: A typical reconstruction from differential measurement; an ensemble averaged reconstruction from differential measurement; a typical reconstruction from direct measurement; and an ensemble averaged reconstruction from direct measurement. True inclusions are plotted with dotted lines and reconstructed inclusions with solid lines.

Based on simulations on 20 realizations, the averaged reconstructed angle is 0.68π and the standard deviation 0.16π for the case with differential measurements. The averaged angle is 0.81π and the standard deviation 0.19π for the case with direct measurements. In each case, the exact angle is $\frac{3\pi}{4}$. The standard deviations on the orientation thus correspond to roughly 20% of error. The reconstruction of the orientation is, however, not as accurate as that of the radius (or equivalently the volume) and the location of the inclusion. The orientation is a finer geometric property of the inclusion and is thus more difficult to observe. Even with differential measurement, our experience is that we can not faithfully reconstruct the orientation of half disks with a radius smaller than 25λ . For direct measurement, we can reconstruct the orientation when the radius of the inclusion is larger than 45λ . Below these numbers, the reconstruction of θ becomes extremely noisy.

4.4 Imaging in the presence of blockers

In all of the above reconstructions, the mean free path is sufficiently small so that the energy leaving the source, hitting the inclusion, and coming back to the detectors without having interacted with the underlying medium, i.e. the energy of the coherent wave field, is relatively small. Inversions based only on the coherent information may thus fail to provide meaningful information about the inclusion. One may however use larger wavelengths, which are less affected by the random medium since the mean free path is much larger as the latter scales like λ^3 . The assumption in Scenarios I and II above is that we have access to wave measurements at frequencies for which there is considerable multiple scattering, i.e., for which the mean free path is relatively small.

There are however situations in which the coherent wave field can hardly be used no matter which frequency we consider, for instance when the inclusion we seek to image is hidden by a large blocker. One can always argue that some energy reaches the hidden inclusion by diffractive effects. Such fields however are quite weak and may well be below noise level as soon as the propagating medium has unknown spatial fluctuations.

In such situations, randomness in the underlying medium may be helpful. In the context considered in this paper of random media with multiple localized scatterers, the

wave energy may be modeled by a radiative transfer equation, and both the blocker and the unknown inclusion may be modeled as constitutive parameters in that equation. We consider here a situation where the blocker is large, spherical, and *known*. It is sufficiently large to block direct paths from the source term to the inclusion. The blocker is treated as any other extended inclusion in the Foldy-Lax and transport models.

We consider the setup shown on the right in Fig. 4. The blocker is located at $(300\lambda, 200\lambda)$ and its radius is 120λ . The inclusion's center and radius are $(300\lambda, 380\lambda)$ and $R = 40\lambda$. All reconstructions are done based on differential measurements, i.e., under Scenario II. The mean free path is estimated in the presence of the known blocker and the inclusion's parameters minimizing (42). Fig. 12 shows reconstructions in random

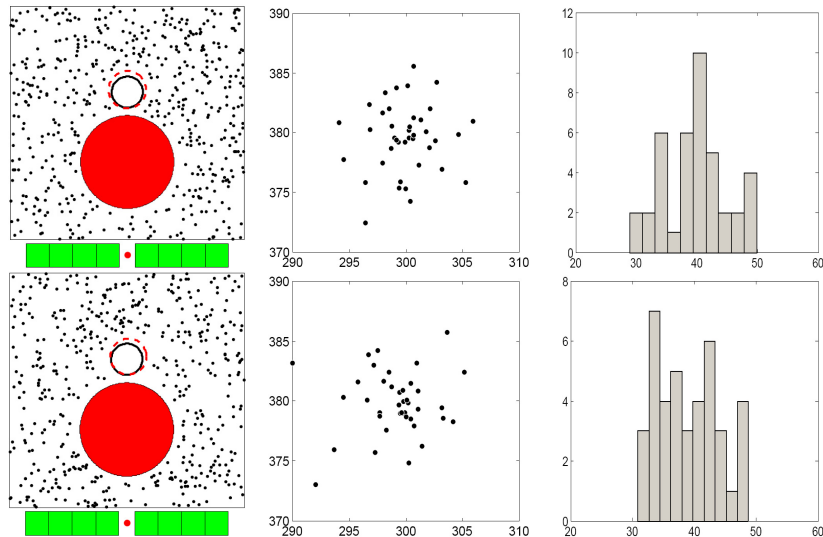


Figure 12: Reconstruction of an inclusion hidden behind a large blocker. Top row: reconstruction in scattering media with $c_0\Sigma^{-1} = 100\lambda$. Bottom row: reconstruction in scattering media with $c_0\Sigma^{-1} = 75\lambda$. From left to right: a typical reconstruction, distribution of the reconstructed locations and histogram of the reconstructed radius.

media with (theoretical) mean free paths equal to $c_0\Sigma^{-1} = 100\lambda$ and $c_0\Sigma^{-1} = 75\lambda$, respectively. In each case, there would be a number of scatterers equal to 6000 on average if the blocker was filled with scatterers so that $l_c \approx 7.75\lambda$. We are therefore in the more stable of the two random media considered so far.

	Inclusion			Reconstruction ^a		
	$c_0\Sigma^{-1}$	location	R	$c_0\Sigma_b^{-1}$	location	R
Medium 1	100	(300, 380)	40	101.0 [2.9]	(299.9 [2.6], 379.6 [2.9])	39.7 [5.3]
Medium 2	75	(300, 380)	40	74.8 [3.3]	(299.1 [3.1], 379.9 [2.6])	39.0 [5.2]

Table 6: Reconstructed mean free path, location and radius in presence of blockers. ^aAverage and standard deviation (numbers in bracket) calculated from 40 reconstructions. All numbers are in units of the wavelength λ .

The average and standard deviations of the reconstructed parameters are shown in Tab. 6. We observe quite good reconstruction capabilities. The images obtained in the

presence of the blocker are of comparable quality to those obtained in the absence of the blocker. Since the blocker is known and not so large so that no energy radiated from the source can reach the inclusion and come back to the array of detectors, this is consistent with what one expects from theoretical considerations.

5 Conclusions

We have derived a radiative transfer equation to model the energy density of mono-frequency waves propagating in random media composed of localized scatters. We have shown the validity of the model based on numerical simulations provided that the medium is sufficiently mixing. In our context, this means that the number of scatterers need be sufficiently large so that sufficient mixing occurs. Otherwise, the energy density becomes statistically less stable, i.e., depends more on the realization of the random medium.

When the medium is sufficiently mixing, the radiative transfer model is sufficiently stable to be used for imaging purposes. Inclusions buried in the random medium are modeled as a constitutive parameter in the transport equation. We have shown numerical evidence that the inverse transport method indeed allows for accurate reconstruction of sufficiently large inclusions from wave energy measurements. Because inverse transport problems are quite ill-posed, in the sense that noise may be drastically amplified during the reconstruction, we have parameterized the inclusion by a small number of parameters, typically its location and its radius for spherical inclusions.

For smaller inclusions whose influence falls below the noise level coming from the statistical instability of the random medium, we have shown that differential measurements, i.e., wave energy measurements in the presence and in the absence of the inclusion, allowed for accurate reconstructions. Because the inclusions are modeled by specular reflections of the wave energy at their boundaries, the inverse model works for inclusions that are significantly larger than the wavelengths. For smaller inclusions, the model needs to be modified and the inclusion treated as a point source in the transport model with an appropriate radiation pattern that depends on geometry (isotropic radiation pattern for a small spherical inclusion).

Acknowledgment

This work was supported in part by DARPA-ONR grant N00014-04-1-0224 and NSF Grant DMS-0239097. GB also acknowledges support from an Alfred P. Sloan Fellowship.

References

- [1] S. R. ARRIDGE, *Optical tomography in medical imaging*, Inverse Problems, 15 (1999), pp. R41–R93.
- [2] M. ASCH, W. KOHLER, G. PAPANICOLAOU, M. POSTEL AND B. WHITE, *Frequency content of randomly scattered signals*, SIAM Rev., 33 (1991), pp. 519–625.

- [3] G. BAL, *Kinetics of scalar wave fields in random media*, Wave Motion, 43 (2005), pp. 132–157.
- [4] ———, *On the self-averaging of wave energy in random media*, SIAM Multiscale Model. Simul., 2(3) (2003), pp. 398–420.
- [5] G. BAL, T. KOMOROWSKI, AND L. RYZHIK, *Self-averaging of Wigner transforms in random media*, Comm. Math. Phys., 242(1-2) (2003), pp. 81–135.
- [6] G. BAL, G. PAPANICOLAOU, AND L. RYZHIK, *Self-averaging in time reversal for the parabolic wave equation*, Stochastics and Dynamics, 4 (2002), pp. 507–531.
- [7] G. BAL AND O. PINAUD, *Time-reversal based detection in random media*, Inverse Probl., 21 (2005), pp. 1593–1620.
- [8] ———, *Accuracy of transport models for waves in random media*, Wave Motion, 43 (2006).
- [9] ———, *Kinetic models for imaging in random media*, (2007). Preprint.
- [10] G. BAL AND L. RYZHIK, *Time Reversal and Refocusing in Random Media*, SIAM J. Appl. Math., 63(5) (2003), pp. 1475–1498.
- [11] G. BAL AND R. VERÁSTEGUI, *Time Reversal in Changing Environment*, Multiscale Model. Simul., 2(4) (2004), pp. 639–661.
- [12] P. BLOMGREN, G. PAPANICOLAOU, AND H. ZHAO, *Super-Resolution in Time-Reversal Acoustics*, J. Acoust. Soc. Am., 111(1) (2002), pp. 230–248.
- [13] L. BORCEA, G. PAPANICOLAOU, AND C. TSOGKA, *Interferometric array imaging in clutter*, Inverse Probl., 21 (2005), pp. 1419–1460.
- [14] R. H. BYRD, P. LU, J. NOCEDAL, AND C. ZHU, *A limited memory algorithm for bound constrained optimization*, SIAM J. Sci. Comput., 16 (1995), pp. 1190–1208.
- [15] J. D. BENAMOU, F. CASTELLA, T. KATSAOUNIS, AND B. PERTHAME, *High frequency limit of the Helmholtz equations*, Rev. Mat. Iberoamericana, 18 (2002), pp. 187–209.
- [16] S. CHANDRASEKHAR, *Radiative Transfer*, Dover Publications, New York, 1960.
- [17] M. CHENEY AND R. J. BONNEAU, *Imaging that exploits multipath scattering from point scatters*, Inverse Probl., 20 (2004), pp. 1691–1711.
- [18] M. CHOULLI AND P. STEFANOV, *Reconstruction of the coefficients of the stationary transport equation from boundary measurements*, Inverse Problems, 12 (1996), pp. L19–L23.
- [19] J. F. CLAERBOUT, *Fundamentals of Geophysical Data Processing: With Applications to Petroleum Prospecting*, Blackwell Scientific, Palo-Alto, 1985.
- [20] D. COLTON AND R. KRESS, *Inverse Acoustic and Electromagnetic Scattering Theory*, Springer-Verlag, New York, 1998.
- [21] L. ERDÖS AND H. T. YAU, *Linear Boltzmann equation as the weak coupling limit of a random Schrödinger Equation*, Comm. Pure Appl. Math., 53(6) (2000), pp. 667–735.
- [22] M. FINK, *Time reversed acoustics*, Physics Today, 50(3) (1997), pp. 34–40.

- [23] L. O. FOLDY, *The multiple scattering of waves*, Phys. Rev., 67 (1945), pp. 107–119.
- [24] V. ISAKOV, *Inverse Problems for Partial Differential Equations*, Springer Verlag, New York, 1998.
- [25] A. ISHIMARU, *Wave Propagation and Scattering in Random Media*, IEEE Press, New York, 1997.
- [26] A. ISHIMARU, S. JARUWATANADILOK, AND Y. KUGA, *Short pulse detection and imaging of objects behind obscuring random layers*, Waves in Random and Complex Media, 16 (2006), pp. 509–520.
- [27] M. LAX, *Multiple scattering of waves*, Rev. Mod. Phys., 23 (1951), pp. 287–310.
- [28] D. LIU, G. KANG, L. LI, Y. CHEN, S. VASUDEVAN, W. JOINES, Q. H. LIU, J. KROLIK, AND L. CARIN, *Electromagnetic time-reversal imaging of a target in a cluttered environment*, IEEE Trans. Antenna Propag., 53 (2005), pp. 3508–3566.
- [29] D. LIU, S. VASUDEVAN, J. KROLIK, G. BAL, AND L. CARIN, *Electromagnetic time-reversal source localization in changing media: experiment and analysis*, IEEE Trans. Antenna Propag., 55 (2007), pp. 344–354.
- [30] J. NOCEDAL AND S. J. WRIGHT, *Numerical Optimization*, Springer-Verlag, New York, 1999.
- [31] J. PRZYBILLA, M. KORN, AND U. WEGLER, *Radiative transfer of elastic waves versus finite difference simulations in two-dimensional random media*, J. Geophys. Res., 111 (2006). B04305.
- [32] K. REN, G. BAL, AND A. H. HIELSCHER, *Frequency domain optical tomography based on the equation of radiative transfer*, SIAM J. Sci. Comput., 28 (2006), pp. 1463–1489.
- [33] L. RYZHIK, G. PAPANICOLAOU, AND J. B. KELLER, *Transport equations for elastic and other waves in random media*, Wave Motion, 24 (1996), pp. 327–370.
- [34] P. SEBBAH (editor), *Waves and Imaging through complex media*, Kluwer, Dordrecht, 2003.
- [35] P. SHENG, *Introduction to Wave Scattering, Localization and Mesoscopic Phenomena*, Academic Press, New York, 1995.
- [36] H. SPOHN, *Derivation of the transport equation for electrons moving through random impurities*, J. Stat. Phys., 17 (1977), pp. 385–412.
- [37] J. SPANIER AND E. M. GELBARD, *Monte Carlo Principles and Neutron Transport Problems*, Addison-Wesley, Reading, Mass., 1969.
- [38] J. R. TAYLOR, *Scattering Theory*, Wiley, New York, 1972.